

Land Surface Albedo Estimation With Chinese GF-1 WFV Data in Northwest China

Hongmin Zhou , *Member, IEEE*, Zhe Wang, Wu Ma, Tao He, *Member, IEEE*, Huawei Wan, Jindi Wang, and Shunlin Liang , *Fellow, IEEE*

Abstract—Land surface albedo (LSA) is one of the driving factors in the energy balance of surface radiation and the interaction between the earth and atmosphere. LSA is an important parameter that is widely used in surface energy balance, medium- and long-term weather forecasting, and global change studies. GF-1 wide field view (WFV) data provide a spatial resolution of 16 m and temporally intensive land surface observations, but efficient algorithm was still lacking for quantitatively land surface parameters estimation. It is essential to improve the data use ability by generating efficient land surface parameter retrieval algorithms. This study proposed an LSA retrieval algorithm by using GF-1 WFV data. Land surface bidirectional reflectance distribution function characteristic parameters were used to represent the non-Lambertian characteristic of land surface. The top of atmosphere (TOA) reflectance is simulated by the 6S radiative transfer model by considering non-Lambertian land surfaces. Linear regression is applied in the TOA reflectance, and LSA is simulated with the surface bidirectional reflectance characteristic parameters to build a lookup table. The proposed algorithm can estimate LSA with high accuracy according to the TOA reflectance without the complex multistep inversion process. The validation results of ground measurements in Northwest China for different land cover types show that the algorithm is effective, and the overall root mean square error was 0.036 when compared with field observation. The algorithm also shows great consistency with Landsat albedo data. The proposed algorithm is of great significance for improving GF data utilization.

Index Terms—GF-1 wide field view (WFV) data, high spatial resolution, land surface albedo (LSA).

Manuscript received March 3, 2021; revised July 30, 2021 and November 9, 2021; accepted December 2, 2021. Date of publication December 20, 2021; date of current version January 12, 2022. This work was supported in part by the National Natural Science Foundation of China under Grant 41801242 and Grant 42090012, and in part by the Key Research and Development Program of China under Grant 2016YFB0501404. (*Corresponding author: Hongmin Zhou.*)

Hongmin Zhou, Wu Ma, and Jindi Wang are with the State Key Laboratory of Remote Sensing Science, Beijing Engineering Research Center for Global Land Remote Sensing Products, Faculty of Geographical Science, BNU, Beijing 100875, China (e-mail: zhouhm@bnu.edu.cn; 202021051071@mail.bnu.edu.cn; wangjd@bnu.edu.cn).

Zhe Wang is with the State Key Laboratory of Remote Sensing Science, Beijing Engineering Research Center for Global Land Remote Sensing Products, Faculty of Geographical Science, BNU, Beijing 100875, China, and also with the School of Surveying & Land Information Engineering, Henan Polytechnic University, Henan 454000, China (e-mail: 211904010004@home.hpu.edu.cn).

Tao He is with the School of Remote Sensing and Information Engineering, Wuhan University, Wuhan 430079, China (e-mail: taohers@whu.edu.cn).

Huawei Wan is with the Satellite Environment Center, Ministry of Environmental Protection, Beijing 100094, China (e-mail: wanhw@secmep.cn).

Shunlin Liang is with the Department of Geographical Sciences, University of Maryland, College Park, MD 20742 USA (e-mail: sliang@umd.edu).

Digital Object Identifier 10.1109/JSTARS.2021.3136852

I. INTRODUCTION

LAND surface albedo (LSA), which refers to the ratio of reflected solar radiation to incident solar radiation, is an important parameter that characterizes the land surface energy balance [1]. LSA provides the boundary conditions at the land–atmosphere interface in the general climate model [2]–[6]. Accurate estimation of LSA is critical in global climate change [7] and polar area research [8]. Many operational remote sensing albedo products are routinely derived from various sensors, such as the Moderate Resolution Imaging Spectroradiometer (MODIS) [9], Polarization and Directionality of the Earth’s reflectance [10]–[13], Medium Resolution Imaging Spectrometer [14], Clouds and the Earth’s Radiant Energy System [12], [13], Meteosat Second Generation [15], [16], Meteosat [17], [18], Visible Infrared Imaging Radiometer Suite [19], [20], and Airborne Visible Infrared Imaging Spectrometer [21]. Their spatial resolutions are mainly of kilometer magnitude, and their temporal resolutions range from daily to monthly. The prevailing LSA products have facilitated a good understanding of global weather change monitoring and detection. However, for regional use, for example, when assessing environmental changes induced by urbanization [22] and land cover change, kilometer-scale resolution LSA products [10], [13], [23] have difficulty capturing patch-size changes that are induced by human activities.

To better understand the characteristics of local and regional climates, Shuai [24] developed a snow-free albedo estimation algorithm based on Landsat surface reflectance and MODIS bidirectional reflectance distribution function (BRDF) information. The algorithm relies on clear-sky MODIS data close to the Landsat acquisition date to produce accurate snow-free albedo estimation; however, they are sometimes not applicable when clear-sky MODIS data are not available and are limited for application after 2000. Gao [25] refined the algorithm by using the surface BRDF information from coarse-resolution products and land cover maps. The availability of concurrent high-quality, clear-sky, and coarse-resolution BRDF data also hindered model application over rapidly changing surfaces. Wang [26] extended the algorithm to retrieve albedo over snow-covered surfaces for snow albedo dynamic analysis from Landsat 8 Operational Land Imager (OLI) data and to monitor the LSA and vegetation dynamics [27]. The only obstacle when using this method is the difficulty in obtaining land surface BRDF information from simultaneous coarse-resolution products, as the MODIS BRDF data were calculated from cumulative 16-day observations,

which assumes that the land surface remained unchanged for 16 days. Although the sixth version heavily improved the weight of the day of interest, the scale effect of the BRDF [28] also induces errors in albedo estimation. For rapid land surface variation detection, He [29] constructed a lookup table (LUT) based on extensive radiative transfer simulation to estimate LSA from Chinese HJ top of atmosphere (TOA) reflectance data directly. The instantaneous TOA reflectance is the only input needed for LSA estimation. Song [30] implemented a recently developed atmospheric correction method, the sensor invariant atmospheric correction, to retrieve surface reflectance from HR-EO (e.g., Sentinel-2 and Landsat-8) TOA reflectance measurements. In his study, both tower-measured albedo and upscaled albedo products were examined at ground based observation for validation stations and used to compare with satellite observations.

The validation accuracy against ground measurements is very high, with an overall root mean square error (RMSE) of 0.03 and r -square (R^2) of 0.947. Later, He [31] extended the LUT estimation algorithm to Landsat multispectral scanner (MSS), thematic mapper (TM), enhanced thematic mapper (ETM), and OLI data to generate long time period high-resolution LSA data. Validation against field observations shows that the approach is effective for both snow-free and snow areas with high accuracy. Zhang [32] improved the estimation by proposing a two-step correction strategy to further reduce the inconsistency between the MODIS BRDF parameters and observed albedo as well as possible spatial resolution differences between MODIS and Landsat data.

With the implementation of the national high spatial resolution Earth observation program, China has launched a series of high spatial resolution Earth observation satellites, such as GF-1, which provides high-precision and wide-range space observation services for global land surface monitoring [33]–[35]. To better use GF series satellite data for quantitative land surface monitoring, more high-quality, high-level land surface product data are needed. In this study, an attempt was carried out to derive a high-quality LSA estimation algorithm from GF-1 wide field view (WFV) data. Although the GF-1 multispectral sensor has a wide field of view (FOV) of 40° , only single angle observation data were available, which makes it difficult to obtain the land surface BRDF characteristics and further hinders LSA estimation based on the BRDF. The LUT algorithm was adopted and improved, and this work will focus on the research area of China, where atmospheric conditions and land surfaces are very complicated.

II. DATA

A. Research Area and Field Observations

The research area of this study is located in Northwest China at 34° – 50° N, 72° – 107° E with a total area of approximately 235×10^4 km². The topography consists mainly of plateaus, basins, and mountains. The high plateaus and mountainous terrain block moist air flow, which lead to a lack of precipitation and arid climate, form the landscape of a vast desert and the Gobi sand beach. The annual precipitation in most areas of Northwest China is less than 500 mm, and this region has continental arid, semiarid, and alpine climates. The land cover from east to the

west is grassland, desert grassland, desert, rocky Gobi, sand dune river, inland lake, and oasis. Affected by human activities, the natural vegetation exhibits a gradually decreasing trend. There are few rivers and lakes in Northwest China, and most are inland rivers and lakes. The area has vast land and abundant natural resources, with a full range of minerals, large reserves, and broad development prospects [36].

The study area has many flux observation towers and meteorological observation towers that were installed for regional-scale hydrological and related ecological process monitoring [37], and instruments for meteorology, radiation, evapotranspiration, soil parameters, and vegetation structure parameters are present on each tower. LSA is measured with CNR4 net radiometers from Kipp & Zonen, The Netherlands, which are placed on the flux observation towers. CNR4 radiometers are located at different heights on different towers with heights of 1.5, 6, and 24 m. The area field observation radius was calculated with the following formula:

$$R = H \cdot \tan\left(\frac{\theta}{2}\right) \quad (1)$$

where R is the radius of the observation area, H is the sensor height, and θ is the effective FOV of the sensor. For CNR4, the FOV was 150° according to the specification. Therefore, the corresponding ground observation areas were approximately $12 \text{ m} \times 12 \text{ m}$, $45 \text{ m} \times 45 \text{ m}$, and $180 \text{ m} \times 180 \text{ m}$, respectively. Radiation was recorded every 10 min, and the ratios of upward and downward shortwave radiation were calculated as the LSA. To ensure time consistency between field observations and satellite data, field observations one-half hour before and after satellite overpass times were averaged. Albedo values less than 0 and larger than 1 were deleted to keep the data reliability. Field observations were downloaded from the National Tibetan Plateau Data Center.¹

Seventeen sites with different land cover types, including grassland, cropland, desert, and wetland, with time series of field observations were selected as our research sites. Among them, seven sites are located in Qinghai Province, five in Gansu Province, and five in Inner Mongolia. Detailed information for all sites is shown in Table I. Fig. 1 shows the time series of field observations for the Dashalong site. It includes two key variables: upward shortwave radiation and downward shortwave radiation.

B. GF-1 Data

In April 2013, the Chinese government launched a high spatiotemporal satellite, GF-1 satellite, and a large number of datasets have been obtained since then. The GF-1 satellite occupies a sun-synchronous orbit at 645-km altitude with a descending node. The overpass time is approximately 10:30 A.M. local time, which is similar to Landsat. The satellite carries two panchromatic/multispectral (P/MS) and four WFV cameras. The four WFV cameras combine a swath of 800 km with a spatial resolution of 16 m, which is significantly better than that of the HJ satellite (another satellite operated by the Chinese government) with a swath of 360 km and spatial resolution of 30 m. In Table II,

¹[Online]. Available: <https://data.tpdc.ac.cn/zh-hans/>

TABLE I
SITE INFORMATION FOR FIELD ALBEDO OBSERVATIONS

Site	Land cover type	Longitude	Latitude	CNR4 Height (m)	Time Period
Dashalong	Grassland	98.9406	38.8399	6	2015-2018
Huangzangsi	Cropland	100.1918	38.2254	6	2015
Yakou	Grassland	100.2421	38.0142	6	2015-2018
Bajitan	Desert	100.3042	38.915	6	2015
Heihe	Grassland	100.4756	38.827	1.5	2015,2018
Arouyangpo	Grassland	100.5204	38.0898	6	2015
JingYangling	Grassland	101.116	37.8384	6	2015-2018
Hunhelin	Cropland	101.1335	41.9903	24	2018
Luodi	Desert	101.1326	41.9993	6	2015
HuYanglin	Cropland	101.1239	41.9932	24	2015
Huangcaogou	Grassland	100.7312	38.0033	6	2015
Shenshawo	Desert	100.4933	38.7892	6	2015
Nongtian	Cropland	101.1338	42.0048	6	2015
Huazhaizi	Desert	100.3201	38.7659	6	2018
Zhangye	Wetland	100.4464	38.9751	6	2018
Ebao	Grassland	100.9151	37.9492	6	2015-2016
Huangmo	Desert	100.9872	42.1135	6	2018

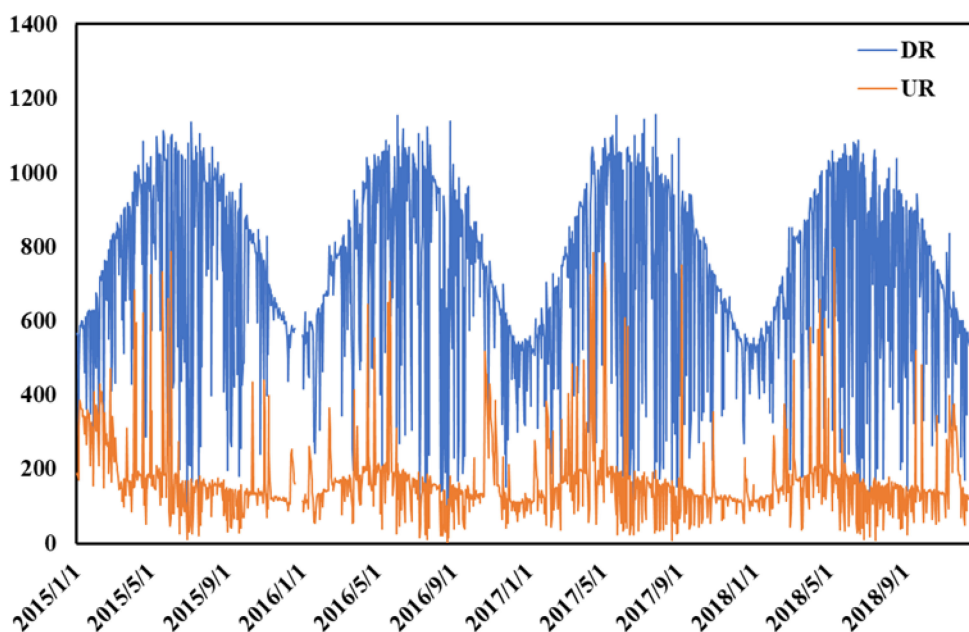


Fig. 1. Time series of field observation at the Dashalong site between January 1, 2015 and December 31, 2018.

TABLE II
BAND SETTING OF GF-1 WFV AND LANDSAT 8 OLI

Satellite	Band	Wavelength (μm)	Satellite	Band	Wavelength (μm)
GF-1 WFV	1	0.45-0.52	Landsat 8 OLI	2	0.45-0.51
	2	0.52-0.59		3	0.53-0.59
	3	0.63-0.69		4	0.64-0.67
	4	0.77-0.89		5	0.85-0.88

we compared the band settings of GF-1 WFV with bands 2–5 of Landsat 8 OLI. The revisit interval is approximately four days at the equator, which is much more frequent than Landsat. The high frequency revisit time, wide coverage ability, and high spatial resolution of the GF-1 satellite make it suitable for large-area and regional land surface monitoring and variation detection.

GF-1 WFV data were collected from the China Centre for Resources Satellite Data and Application (CCRSDA).² In the process of searching remote sensing images, we first determined the spatial location according to the study area and then determined the time range of the required remote sensing images. Finally, to maintain the accuracy of the estimation, we selected remote sensing images with cloud cover less than 10%. We think that remote sensing images with less than 10% cloud cover can be regarded as clear-sky data. For the 17 stations, we collected a total of 176 images of GF-1 WFV L1A level data obtained from 2015 to 2018. There were 119 images of grassland, 28 images of cropland, 26 images of desert, and three images of wetland. Since aerosol effects were considered in the atmospheric radiative transfer simulation in the proposed method, atmospheric corrections were not required. Geometric corrections were applied according to the Landsat OLI data.

C. Landsat Data

The Landsat series is jointly managed by the National Aeronautics and Space Administration (NASA) and United States Geological Survey (USGS). Eight satellites have been launched since 1972. Landsat sensors of Landsat 1-5 were MSS sensors, Landsat 4 and 5 were also equipped with a TM sensor, Landsat 7 was equipped with an ETM+ sensor, and Landsat 8 was equipped with OLI and TIRS sensors. Landsat 7 was launched on April 15, 1999, and ETM+ is an eight-band sensor that covers a range of wavelengths from infrared to visible light. Compared with the Landsat 5 TM sensor, ETM+ has a 15-m resolution band, which has higher resolution in the infrared band. Since May 31, 2003, the Landsat 7 scanner corrector has acted abnormally, and the data can only be calibrated using the SLC-off model. The Landsat 8 satellite was launched on February 11, 2013 and was equipped with OLI and TIRS. The OLI passively senses both reflected solar radiation and emitted thermal radiation from the Earth's surface and has nine sensor bands that cover a range of wavelengths from infrared to visible light. Compared with the ETM+ sensor of the Landsat 7 satellite, OLI adds a blue band (0.433–0.453 μm) and shortwave infrared band (1.360–1.390 μm). The blue band is mainly used for coastal zone observations, and the shortwave infrared band includes strong water vapor absorption characteristics, which can be used for cloud detection. TIRS is the most advanced and best-performing thermal infrared sensor developed thus far. TIRS can collect heat loss data from the Earth with the goal of understanding water consumption in the observed area, especially in arid regions.

The Landsat data is used for intercomparison with GF-1 to verify the estimation algorithm. Landsat 7/8 L1T data were downloaded from the USGS archives³ and were corrected to

atmospheric top reflectance by using the radiometric correction coefficient. Geometric corrections were not required due to the high accuracy of geometric alignment of Landsat data. Clear-sky data with less than 10% clouds were selected to calculate the broadband albedo. In this study, we downloaded a total of 31 Landsat image scenes that corresponded to the stations and times of the GF satellite data. Landsat albedo data were estimated according to He [31] and were used to verify relative accuracy.

III. ESTIMATION ALGORITHM

The method proposed in this study is an empirical method for estimating broadband LSA with TOA reflectance. Two aspects were referred: first, forward simulate the TOA reflectance with radiative transfer model based on the land surface BRDF and LUT construction; second, estimate LSA based on LUT according to the observation geometry of GF-1 WFV data. Fig. 2 shows the flowchart of the estimation algorithm.

The forward simulation and LUT construction consists of the following main steps:

- 1) Extraction of BRDF model parameters for different surface types from the MODIS MCD43A1 products;
- 2) Establishment of GF-1 WFV and MODIS band conversion relationships from hyperspectral feature library data and sensor spectral response functions;
- 3) Calculation of surface albedo based on the characteristic parameters of ground bidirectional reflectance;
- 4) Simulation of TOA directional reflectance under geometric and atmospheric conditions using the second simulation of the satellite signal in the solar spectrum (6S) radiative transfer model;
- 5) Establishment of a lookup table between TOA reflectance and surface albedo.

A. Land Surface BRDF Characteristic Description at the GF Scale

Land surface BRDF is critical for accurate albedo estimations. To better understand the land surface bidirectional reflectance characteristics, BRDF at the GF scale is needed. However, due to the single angle observations of GF-1 WFV data, no BRDF product is available so far. Based on the assumption that the homogeneous land surface has the same BRDF characteristics at different scales [24], BRDF data from MODIS pure pixels (determined at Landsat scale), which were considered homogeneous at different scales, were adopted to represent the GF-scale BRDF characteristics. MODIS MCD43A data, which are BRDF/albedo model parameters, were transferred with a band-transfer function to the GF-1 WFV bands.

A total of 245 surface hyperspectral reflectance data points were selected from the USGS, advanced spaceborne thermal emission and reflection radiometer spectral libraries, and moderate resolution atmospheric transmittance and radiance code simulation data.

The band transfer coefficients of MODIS and GF-1 WFV were calculated with the least square method. The band reflectance of MODIS and GF-1 were calculated according to their band response functions with formula 1; therefore, for each spectral

²[Online]. Available: <http://www.cresda.com/CN/>

³[Online]. Available: <https://earthexplorer.usgs.gov/>

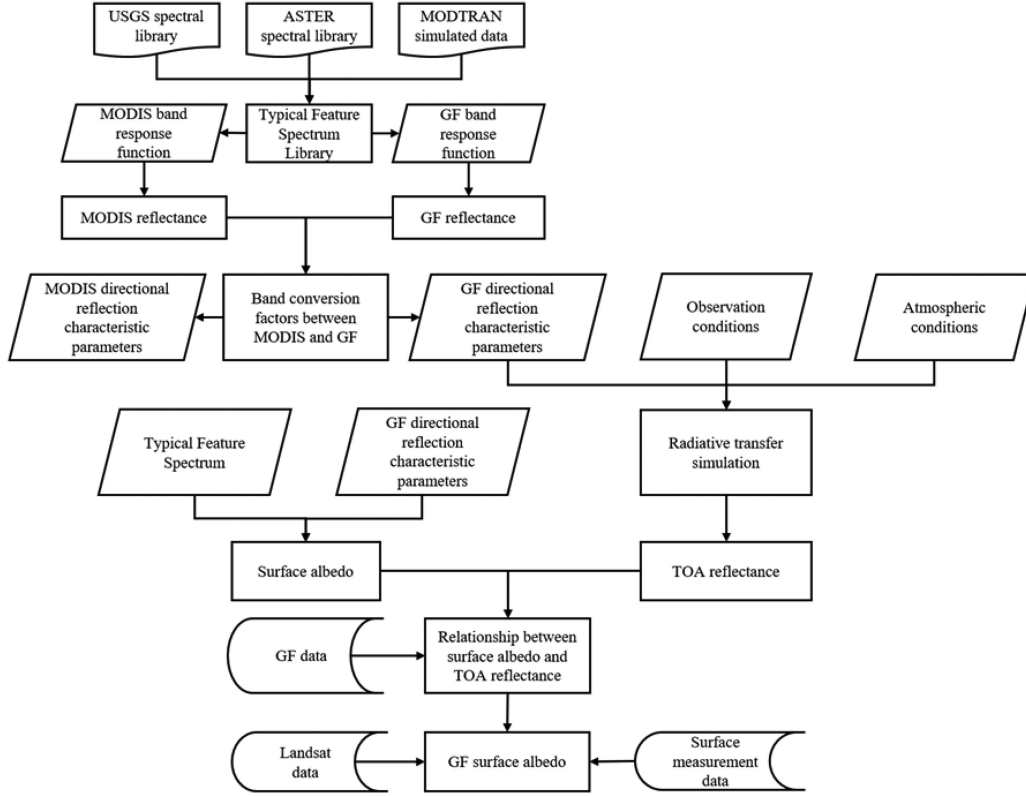


Fig. 2. Flowchart of the GF-1 WFV LSA estimation algorithm.

reflectance data, MODIS and GF-1 band reflectance were calculated. Then, the least square method was applied to calculate the band transfer coefficient. Table III shows the band transfer coefficient from MODIS to GF-1

$$\rho_{\lambda} = \int_{\lambda_1}^{\lambda_2} f_i \rho_i d\lambda_i \quad (2)$$

where λ is the band setting of the sensor, f_i is the band response function of the sensor, and ρ_i is the hyperspectral reflectance in the band response range.

The band transfer coefficient was then used to transfer the MODIS BRDF parameters to the GF-1 band. One thousand BRDF data samples, which represent different vegetation types, soil, snow, and water, were transferred to the GF-1 WFV bands.

B. Surface Albedo Calculations

LSA is also the integration of bidirectional reflectance. The LSA required in the lookup table establishment process was estimated from the surface directional reflectance characteristic parameters. Black/white sky albedo (BSA/WSA) was calculated from the BRDF/albedo model parameters according to Schaaf *et al.* [38]

$$\begin{aligned} \alpha_{bs}(\theta, \lambda) = & f_{iso}(\lambda) (g_{0iso} + g_{1iso}\theta^2 + g_{2iso}\theta^3) \\ & + f_{vol}(\lambda) (g_{0vol} + g_{1vol}\theta^2 + g_{2vol}\theta^3) \\ & + f_{geo}(\lambda) (g_{0geo} + g_{1geo}\theta^2 + g_{2geo}\theta^3). \end{aligned} \quad (3)$$

Coefficients in the formula are shown in Table IV.

C. TOA Reflectance Simulation

The 6S radiative transfer model is an improved version of the simulation of the satellite signal in the solar spectrum (5S) model that was developed by Tanre *et al.* [39] and is widely used for atmospheric corrections of remote sensing images. The 6S radiative transfer model describes atmospheric images of sunlight that are subjected to the entire transmission path of the sun-ground target-remote sensor under different scenarios.

In the 6S radiative transfer model, the atmosphere is considered to vary only in the vertical direction while remaining consistent in the horizontal direction, and the model divides the surface into uniform and nonuniform Lambertian and three types with directional reflection characteristics. When the surface is non-Lambertian, the contribution of the ground target to the signal received by the remote sensor at the top of the atmosphere can be divided into the following four parts.

- 1) Light is incident directly to the ground and is reflected directly from the ground to the remote sensor.
- 2) Light is scattered by the atmosphere to the ground and is reflected directly from the ground to remote sensors.
- 3) Light is incident directly to the ground and is reflected by the ground and then scattered by the atmosphere to remote sensors.
- 4) Light is scattered to the ground by the atmosphere and then to remote sensors by ground reflection and atmospheric scattering, and the ground and atmosphere scatter each other many times to reach the remote sensor.

TABLE III
BAND CONVERSION FACTORS FROM DOMESTIC SATELLITES TO MODIS

	MODISb1	MODISb2	MODISb3	MODISb4	MODISb5	MODISb6	MODISb7	offset
GF1-WFV1-b1	0.020658	-0.022008	0.871463	0.126543	0.007873	0.004235	-0.003502	0.000716
GF1-WFV1-b2	0.084125	-0.008055	0.095824	0.823900	0.012172	-0.012718	0.006473	0.000782
GF1-WFV1-b3	1.020992	0.018103	-0.005118	-0.033132	-0.007866	0.018849	-0.009392	-0.000708
GF1-WFV1-b4	-0.046859	1.031795	-0.039427	0.099816	-0.074942	0.017655	0.011467	-0.000546
GF1-WFV2-b1	0.022013	-0.027772	0.822645	0.178221	0.011630	0.003454	-0.003957	0.000940
GF1-WFV2-b2	0.115406	-0.006635	0.059467	0.828667	0.010604	-0.014377	0.007470	0.000799
GF1-WFV2-b3	1.024441	0.017976	-0.004178	-0.037712	-0.007582	0.019271	-0.009604	-0.000731
GF1-WFV2-b4	-0.040795	1.039829	-0.034911	0.090094	-0.091245	0.027112	0.008683	-0.001068
GF1-WFV3-b1	0.017386	-0.024995	0.831289	0.171878	0.010472	0.002601	-0.002753	0.000792
GF1-WFV3-b2	0.170340	-0.005451	0.029080	0.803709	0.010228	-0.017617	0.009060	0.000898
GF1-WFV3-b3	1.040827	0.032475	-0.038057	-0.033561	-0.014576	0.030990	-0.017950	-0.000876
GF1-WFV3-b4	-0.054761	1.036835	-0.043214	0.112658	-0.083020	0.018843	0.013174	-0.000374
GF1-WFV4-b1	0.023865	-0.023965	0.863700	0.132725	0.008718	0.005092	-0.004730	0.000839
GF1-WFV4-b2	0.148917	-0.009994	0.073766	0.783493	0.013046	-0.017189	0.008547	0.000942
GF1-WFV4-b3	1.042176	0.032263	-0.038401	-0.034479	-0.014400	0.030937	-0.017978	-0.000869
GF1-WFV4-b4	-0.045277	1.024831	-0.037415	0.093653	-0.059549	0.010675	0.012493	-0.000497

TABLE IV
ESTIMATED SURFACE ALBEDO FACTORS

Parameters	k=iso	k=vol	k=geo
g _{0k}	1	-0.007574	-1.284909
g _{1k}	0	-0.070987	-0.166314
G _{2k}	0	0.307588	0.041840
White-sky	1	0.189184	-1.377622

The TOA reflectance can be expressed as

$$\begin{aligned} \rho_{\text{toa}} = & \rho_0 + T_g [e^{-\tau/\mu_v} e^{-\tau/\mu_s} \rho_s \\ & + e^{-\tau/\mu_v} t_d(\mu_s) \bar{\rho} + e^{-\tau/\mu_v} t_d(\mu_v) \bar{\rho}' + t_d(\mu_s) t_d(\mu_v) \bar{\bar{\rho}} \\ & + \frac{(e^{-\tau/\mu_s} + t_d(\mu_s))(e^{-\tau/\mu_v} + t_d(\mu_v)) S(\bar{\rho})^2}{1 - S\bar{\rho}}] \end{aligned} \quad (4)$$

where ρ_{toa} is the reflectance observed by the remote sensor at the top of the atmosphere; ρ_0 is the atmospheric path radiation reflectance; ρ_s is the surface reflectance; S is the hemispheric reflectance downward from the bottom of the atmosphere; μ_s is the cosine of the solar zenith angle; μ_v is the cosine of the satellite zenith angle; $e^{-\tau/\mu_s}$ and $t_d(\mu_s)$ are the direct solar light reaching the ground and atmospheric transmittance via atmospheric diffuse light reaching the ground, respectively; $e^{-\tau/\mu_v}$ and $t_d(\mu_v)$ are the atmospheric transmittance for direct ground reflections from the observation direction to the remote sensor and for diffuse atmospheric light reaching the remote

sensor, respectively; τ is the atmospheric attenuation coefficient; and $\bar{\rho}$, $\bar{\rho}'$, and $\bar{\bar{\rho}}$ depend on atmospheric optical parameters and surface reflectance. They are the hemispherical reflectance of the atmosphere scattered to the ground, surface hemispherical reflectance scattered to the atmosphere by the ground, and surface hemispherical reflectance after two scatterings from the atmosphere and ground, respectively. T_g is the absorptivity rate of O_3 , H_2O , and other gases in the atmosphere to the visible and near-infrared bands.

In this study, we used the 6S model to forward and simulate the TOA directional reflectance that is needed for LUT construction. Input parameters include geometric parameters, atmospheric model, aerosol type, aerosol optical thickness, altitude, sensor height, spectral parameters, surface reflectivity type, and atmospheric correction method. To simulate the TOA directional reflectance under different conditions, the input parameters were organized into input files that were cyclically recalled for simulating the atmospheric top directional reflectance under different conditions. The input parameters and parameter settings for simulating TOA reflectivity under different conditions when using the 6S radiative transfer model are shown in Table V.

D. LUT Construction

Based on the estimated LSA and TOA reflectance, a lookup table was constructed. The lookup table was built primarily on the input parameters that were available from GF-1 WFV observations. In this term, the lookup table was built mainly

TABLE V
CONFIGURATIONS FOR SIMULATING SURFACE ALBEDO AND TOA
REFLECTANCE DATA

Parameters	Values
Solar zenith angle	0, 5, 10, 15, ..., 75
View zenith angle	0, 5, 10, 15, ..., 40
Relative azimuth angle	0, 30, 60, ..., 180
Atmospheric model	Tropic, Mid-latitude summer, Mid-latitude winter, Subarctic summer, Subarctic winter, United States standard
Aerosol optical depth type	Continental
Aerosol optical depth	0.05, 0.1, 0.15, 0.2, 0.25, 0.3, 0.35, 0.4

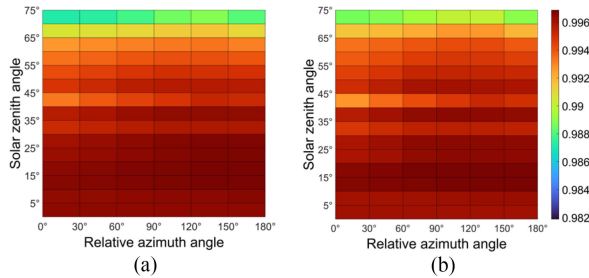


Fig. 3. Distribution of fitted decision factors. (a) BSA. (b) WSA.

on the basis of the observed geometric information, such as solar zenith angle, view zenith angle, and relative azimuth angle. According to the simulation intervals, solar zenith angles and view zenith angles of 5° intervals relative azimuth angles of 30° interval bins were constructed and to establish a search grid, a $15 \times 9 \times 7$ three-layer LUT was built.

A linear regression method was used to calculate the lookup coefficients for each grid. Fig. 3 shows the determination coefficient variations of BSA and WSA with solar zenith angle and relative azimuth angle. Fig. 3 shows that the regression accuracy was higher at small solar zenith angles than at large solar zenith angles, while the variation pattern was not obvious according to the relative azimuth angle. Although the determination coefficient varies according to solar and view angles, the values were always larger than 0.98, which indicates that the regression accuracy was high and that the lookup table accuracy can be considered acceptable.

Figs. 4 and 5 show scatter plots of the albedos that were calculated with the method in Section III-B and LUT for the minimum and maximum solar/view angles. For small angles, the regression accuracy was very high, with R^2 values greater than 0.995 and RMSE values less than 0.02. The accuracy of the fit decreased with increasing solar and observation angles. When the solar zenith angle was a maximum of 75° , the observation zenith angle was 40° of the maximum observation angle of

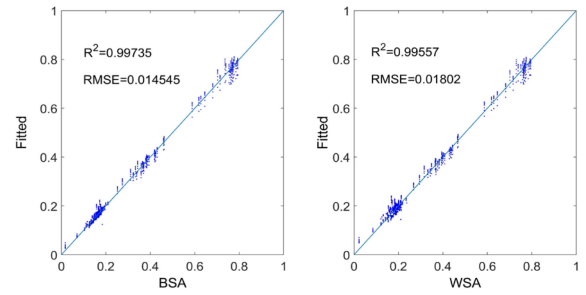


Fig. 4. $0^\circ-0^\circ-0^\circ$ angle condition fit results. The X-axes are calculated BSA and WSA with formula 1 and the Y-axis are fitted BSA and WSA with the LUT.

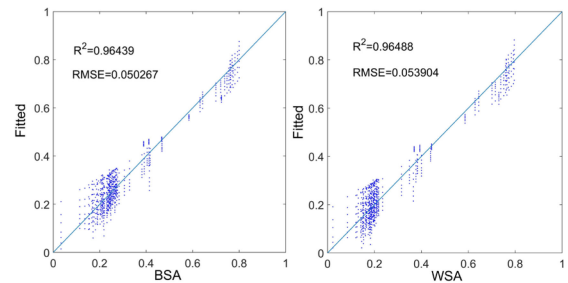


Fig. 5. $75^\circ-40^\circ-180^\circ$ angle condition fit results. The X-axes are calculated BSA and WSA with formula 1 and the Y-axes are fitted BSA and WSA with the LUT.

the GF, and the relative azimuth was 180° . The BSA/WSA fit coefficients of determination were all approximately 0.964, and the RMSEs were all approximately 0.05.

E. LSA Estimation With LUT

The model used in this article includes two parts: establishing the relationship between TOA reflectance and surface albedo through radiative transfer model, and then establishing an LUT; Albedo is calculated by LUT. Each image has different solar zenith angle and view zenith angle. Then we find the corresponding grid from the LUT according to these angles. Finally, the surface albedo is calculated according to the coefficients in the grid. The formula is as follows:

$$\alpha_{\text{albedo}} = a_1 \times t_1 + a_2 \times t_2 + a_3 \times t_3 + a_4 \times t_4 + b \quad (5)$$

where α_{albedo} is the surface albedo, a_n and b are the coefficients in the LUT, and t_n is the TOA reflectance of different bands.

IV. RESULTS

A. Validation Against Ground Measurements

The estimated albedo was compared with field observations. The blue sky albedo is the weighted average of BSA and WSA with the direct-diffuse radiation ratio according to Chen and Lucht [40], [41]. Because of the strong correlation between albedo and land cover type [42], the sites were categorized according to land cover types for validation, i.e., grassland, cropland, desert, and wetland. The results are shown in Fig. 6. As the scatter plot shows, the estimates are distributed along the

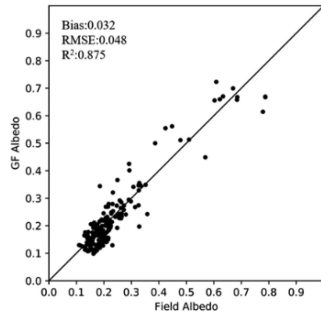


Fig. 6. Validation against ground measurements.

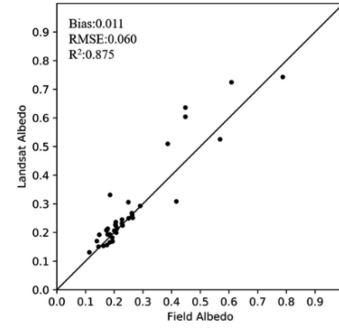


Fig. 8. Comparison of Landsat albedo and surface result.

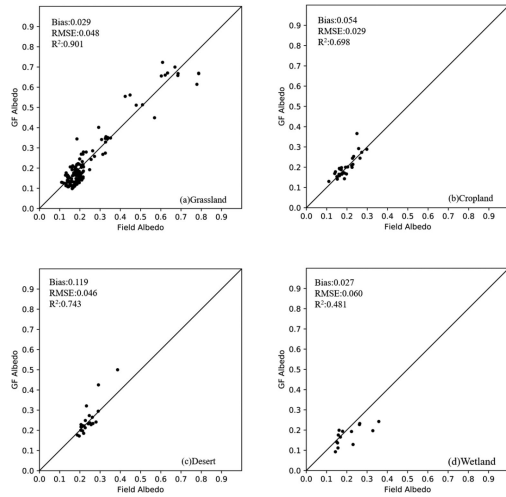


Fig. 7. Comparisons of GF-1 WFV albedo and surface results in the experimental area of (a) grassland sites, (b) cropland sites, (c) desert sites, and (d) wetland sites.

1:1 line, and high accuracy was reached with R^2 values of 0.875 and RMSEs of 0.048 for all sites.

For different land cover types, the proposed method performed similarly, with an R^2 range of 0.481–0.901 and RMSE range of 0.029–0.060 (Fig. 7). The grassland sites had the most GF-1 WFV data; so the reliability of the results was high. Points in the figure with albedos larger than 0.7 were due to the presence of snow on the ground surface, which indicates that the proposed algorithm was capable of snow-cover albedo estimations.

Among the four land cover types, the best albedo estimation results were obtained for farmland, which had RMSE and R^2 values of 0.029 and 0.698, respectively. The albedo of farmland varied between 0.1 and 0.3 (except at the snow-covered points). Farmland was mostly affected by anthropogenic activities. The proposed algorithm estimated LSAs based on instantaneous satellite observations and is capable of capturing abrupt land surface changes in terms of albedo.

From the scatter plot, the albedo of desert and wetland changed little: the albedo of desert was between 0.2 and 0.5 and that of wetland was between 0.1 and 0.2. Although clustering of albedo values reduced the determination coefficient to some degree, estimation accuracy was still very high, with R^2 values of 0.743 and 0.481, and RMSE values of 0.046 and 0.060, respectively.

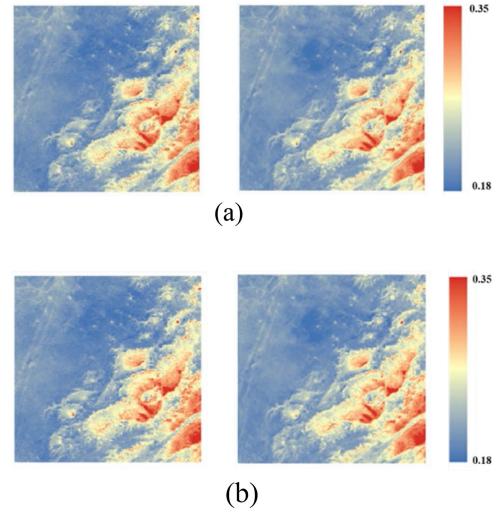


Fig. 9. Comparisons of GF-1 WFV and Landsat 8 BSA and WSA estimates at Luodi Station. (a) BSA. (b) WSA.

B. Validation Against Landsat Estimation

According to network observations, Landsat albedo was verified to have high accuracy. In this study, the Landsat albedo data were highly consistent with field observations, with an RMSE of 0.060 and R^2 of 0.875 (Fig. 8). The regional estimation was compared with Landsat albedo on adjacent dates. The points with albedo greater than 0.4 in the figure are snow-covered points because the surface observation radiometer was affected by snow cover, which may lead to poor consistency between the estimated and ground measurement results.

The GF-1 WFV albedo on February 23, 2015 (DOY = 54), around the Luodi site was compared with the Landsat albedo on February 24, 2015 (DOY = 55), as shown in Fig. 9. Albedo values of a 6 km × 6 km area around the observation tower were compared, and the land cover types included bare soil, grassland, and cropland. In the regional albedo map, high albedo values were due to the existence of snow cover in February. The results show that there was good spatial consistency between the GF-1 WFV and Landsat estimates. We compared the BSA and WSA of GF-1 WFV and Landsat, respectively, and the scatter plot is shown in Fig. 10. According to the scatter plot, the correlation coefficients of BSA and WSA were very high, both were greater than 0.896, and both RMSEs were limited to 0.01–0.02. For

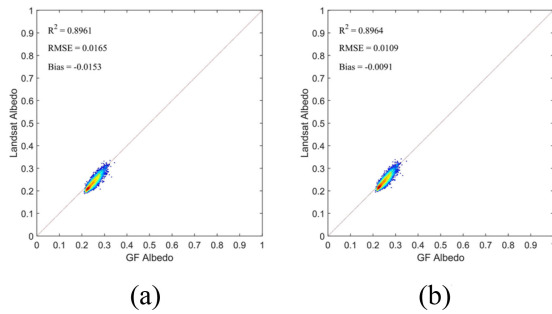


Fig. 10. Scatter plots of BSA and WSA of GF-1 WFV and Landsat 8 at Luodi station. (a) BSA. (b) WSA.

BSA, GF estimation results were slightly lower than those of Landsat 8, and the bias was -0.015 ; for WSA, GF estimation results were also slightly lower than those of Landsat 8, and the bias was -0.009 . The comparative results of the GF-1 WFV and Landsat WSA and BSA were very close, but the overall results of the WSA were slightly better than those of BSA. This may have been because the two satellites had different acquisition times, while the daytime albedo was theoretically independent of the solar zenith angle and therefore independent of acquisition time, and the WSA was better estimated [29].

C. Validation With Wang's Estimation Method

To validate the estimation algorithm proposed in this study, Shuai's [24] and Wang's [27] method was adopted to estimate GF albedo and compared with field observations and the proposed method. Radiation and atmospheric correction were first applied to GF-1 WFV L1 data to obtain directional surface reflectance data. Radiation correction was performed according to the radiation coefficient broadcasted by the CCRSDA, and atmospheric correction was applied with the ENVI. High-quality MODIS BRDF data (MCD43A2 products, sixth version) synchronized with GF-1 observation time were downloaded from the Application for Extracting and Exploring Analysis Ready Samples. Considering that the land surface of the tower site was homogeneous, MODIS BRDF parameters were directly used to represent the BRDF characteristics of GF-1 pixels. GF-1 was directional observations, while Landsat was considered nadir observations; so an albedo-to-directional (AD) reflectance ratio was calculated similar to Wang's albedo-to-nadir (AN) reflectance ratio. The band settings of GF-1 and MODIS were significantly different; so the GF-1 band was transferred to MODIS based on the previous 245 surface spectral reflectance data. Broadband albedo was calculated with the band transfer model proposed by [43].

Fig. 11 shows the result of GF-1 albedo estimated with the method of Shuai and Wang. Compared with field observations, the albedo calculated by the method of Shuai and Wang consisted of field data with RMSE of 0.058 and bias of 0.102. The main reason for the deviation may be as follows. In the method of Shuai and Wang, Landsat data, which were considered nadir observations, and the spectral AN were used. In fact, the vertical observation was relatively stable, and the nadir reflectance data were more representative. In contrast, due to

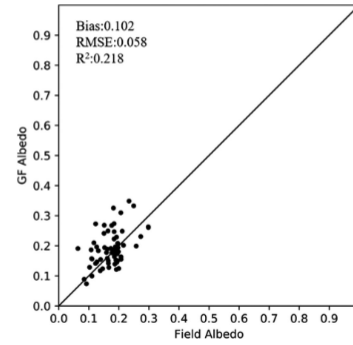


Fig. 11. Comparison of GF albedo and surface result.

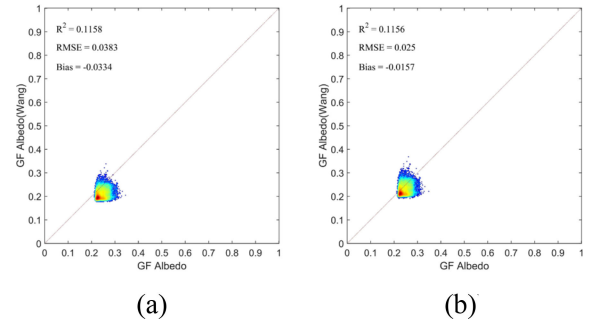


Fig. 12. Scatter plots of BSA and WSA of two methods at Luodi station. (a) BSA. (b) WSA.

the different observation angles of GF-1 data, the observation direction differed from pixel to pixel, which may have decreased the representativeness of the ratio in different pixels. The other way to obtain the AN is to convert GF-1 directional reflectance to nadir reflectance according to the MODIS BRDF data. In this way, the error of BRDF data will be further introduced into the nadir reflectance. Thus, in this study, AD was used.

Fig. 12 shows the scatter density map of GF-1 albedo derived from the proposed algorithm and the method of Shuai and Wang. It can be seen from the figure that albedo generated with the two estimation methods was weakly correlated. Both BSA and WSA were better when the albedo value was low; when albedo increased, the consistency decreased. Overall, albedo from the method of Shuai and Wang was underestimated when compared with the LUT estimation algorithm with a bias of -0.0334 for BSA and -0.0157 for WSA.

D. LSA Time Series Estimation

By benefitting from the high-revisit cycle of the GF-1 satellite, time series albedo mapping is possible. Fig. 13 shows the time series surface albedo monitoring results at the Heihe research area (38.827°N , 100.4756°E) in a $3\text{ km} \times 3\text{ km}$ area in 2015. The area around the Heihe Experimental Station is dominated by farmland and grassland. Fig. 13 shows that the albedo time series can be monitored with GF-1 WFV data. LSA was characterized by an overall trend of decreasing and then increasing during the year, which was mainly related to the season. Among them, the albedos of 20150109, 20150125, 20151219, 20151223, and 20151231 were higher because of snow cover. Since the area

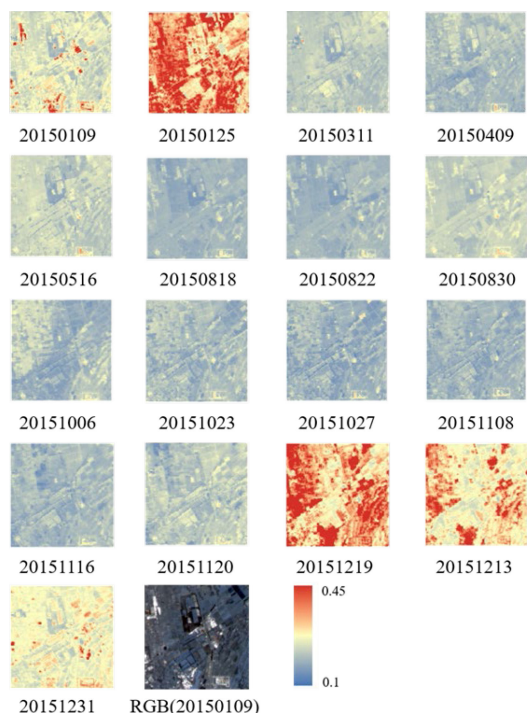


Fig. 13. Temporal variation chart of albedo for the Heihe research area of 2015.

around the Heihe site is dominated by agricultural land, changes in surface albedo values were related to crop growth patterns, e.g., albedo gradually decreased when crops were planted starting in May; crops reached their most vigorous growth stage in August, which corresponded to the lowest albedo; and albedo increased when crops were harvested in October. The albedo changes all corresponded to the actual phenological situation. The albedo results that were obtained from ground observation data in one year were compared with the GF-1 WFV surface albedo estimation results, and a time series of albedo variations was plotted (Fig. 13). Fig. 14 shows that the surface albedo of nearly all sites varied significantly with season. From November to February, the surface albedo was relatively high and varied greatly, while the albedo from May to October was relatively stable (i.e., remaining between 0.1 and 0.3). Since our study area is located in northwestern China at a high altitude and has an arid/semiarid climate, snow accumulation often occurs in winter; so winter albedo often varies significantly. Over the year, the surface albedo usually reaches its highest value in winter and lowest value in summer because the presence of snow in winter increases the albedo, while the vegetation in summer is relatively luxuriant and the albedo is low. Liang [44] indicated that the region with the greatest seasonal variations in albedo lies between 30°N and 90°N and that the variations are due to changes in snowfall and vegetation phenology, which was in strong agreement with our results. We also found that most surface albedo estimates were slightly lower than those of the ground observations. These underestimations and deviations may have been due to various errors in the estimation process, which will be described in detail in Section V. Among these sites,

the Huyanglin site did not experience large changes in albedo throughout 2015 and maintained normal levels between 0.2 and 0.3 even in winter, which were probably due to the absence of snowfall near the site during the winter of that year.

V. DISCUSSION

A. Errors Induced by Land Surface Heterogeneity

Surface albedo is strongly correlated with land cover type [42]. Due to different combinations of vegetation and background soil composition, uncertainties in validations of surface albedo can be affected by increased surface heterogeneity. Additionally, the spatial representation of some stations may be poor, which would result in deviations in albedo estimation results. Some sites have poor spatial homogeneity, which leads to increased errors in surface albedo estimation results. The study by Cescatti *et al.* [45] concluded that geostatistical properties obtained from high-resolution scenes confirm that the observed mismatches in grasslands and agricultural fields may be due to the extreme fragmentation of these landscapes. In further studies, the bias of albedo estimations in croplands and grasslands was low, while that in desert was high (bias: 0.067; RMSE: 0.020). We believe that this bias was related to vegetation cover. The results of this study are in good agreement with the findings of a previous study that used HJ satellite data to estimate albedo [29]. The results showed that the bias and RMSE values of forest sites were the lowest. With a decreased vegetation canopy fraction, the surface albedo gradually increased, and the deviation and RMSE were larger.

B. Errors Induced by Snow Cover

In alpine mountainous areas, an increase in snow albedo will lead to a serious loss of surface radiation energy, weaken convective exchange, and eventually lead to decreased precipitation. At the same time, snow albedo also affects snow melting, which is an important factor for seasonal snow cover changes. Due to the high albedo of snow, snow albedo inversion has become a major challenge and major source of error in surface remote sensing albedo inversions. Because data from snow-covered areas are included in the data used, the albedo estimation exhibited overestimations for snow-covered surfaces. The study by He *et al.* [31] indicated an overestimation of snow albedo as high as 0.05. Tekeli *et al.* [46] found that the MODIS snow albedo daily (SAD) product overestimates snow albedo by approximately 10% based on albedo data observed from automatic weather stations and compared it with the MODIS SAD snow product.

C. Errors Induced by Aerosol Types

Aerosol scattering is the main atmospheric factor that affects visible radiation. The default “continental” aerosol type used in this study may lead to overestimation of albedo results. He *et al.* [31] changed the default “continental” aerosol to “biomass burning” and “urban” aerosols for some SURFRAD stations and found that the accuracy of albedo estimations varied among different sites and that the RMSE differences were less than 0.004. By modifying different aerosol types, the accuracy of albedo

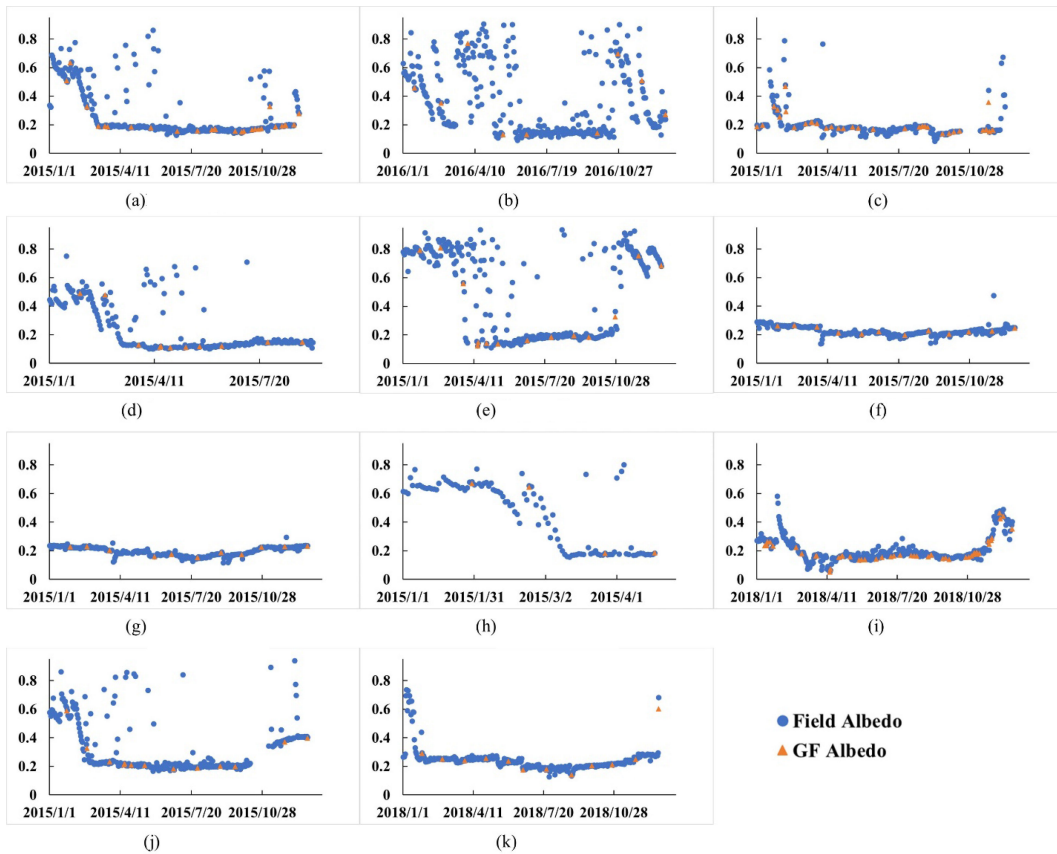


Fig. 14. Albedo estimation results of the time series in each study area within one year.

estimations varies among different stations, which indicates that albedo estimations in nondesert areas may be improved with an accurate aerosol type map [42]. Water vapor content also affects shortwave radiation in ground-based measurements; so including a correction for water vapor content may help to further improve shortwave albedo estimates [31].

High spatial–temporal resolution and wide coverage make it possible to capture and understand small-scale and large-scale biological, chemical, and physical processes. However, precise radiometric corrections are required before satellite signals can be connected to any biophysical and biochemical parameters [47]. Due to the lack of satellite calibrators on GF-1 satellites, the CCRSDA conducted a field survey at the Dunhuang calibration site in August 2014 and updated the field-measured radiation coefficient in October 2014. The calibration accuracy of the GF-1 WFV sensor may also be a major factor in the increased uncertainty in albedo estimations. For consistency and calibration accuracy among cameras, the research by Feng and Li [48] indicated that the radiometric calibration accuracy of high spatial resolution satellites needs further improvement. To further improve surface albedo estimates, refinement of radiometric calibrations is a feasible approach.

VI. CONCLUSION

LSA data are important for climate change, agricultural monitoring, urban change, and land resource studies. The launch of the GF series of high-resolution Earth observation satellites

provides frequent observations of land surfaces at a spatial resolution of 16 m. To improve the efficiency and ability of data use, this article presents a method to estimate LSA by using high spatial and temporal resolution GF-1 WFV data. This method uses the characteristic parameters of MODIS surface bidirectional reflection to represent the real situation of non-Lambertian surfaces. A 6S radiative transfer simulation model was applied to simulate the TOA directional reflectance, and a linear regression model was built with simulated TOA reflectance and LSA that were estimated from surface bidirectional reflection characteristics to construct an LSA estimation model. The method proposed in this article discards the complex multistep inversion process and directly establishes the statistical relationship between TOA reflectance and LSA. However, the method still has limitations. We used clear-sky data; so we can only calculate clear-sky albedo.

Comparing the estimation results with field observations shows that the estimations had high accuracy with an R^2 of 0.875 and RMSEs of 0.048 for all land cover types. When compared with Landsat data, this method can generate more accurate albedo results, with an R^2 of 0.875 and RMSE of 0.060. When compared with Wang’s method, this method can generate more accurate albedo results, with an R^2 of 0.218 and RMSE of 0.058. This indicates that the proposed method is effective for use with different land cover types. Moreover, depending on the high-revisit frequency of the GF satellite, the LSA time series in the Heihe study area were estimated in 2015. The results reflect the annual variation characteristics of LSA well,

which are completely consistent with the phenological variation characteristics in this area. In addition, slight biases of estimation results in different land cover types were also found.

There are some drawbacks in this study. MODIS-scale land surface BRDF data were used directly in this study to represent the GF-1 scale land surface bidirectional reflectance characteristics due to the lack of the multiangle reflectance product of GF-1 WFV data. The scale mismatch of GF-1 and MODIS data was ignored. For more accurate LSA estimations of GF-1 WFV data, proper scale transformation should be considered in the land surface BRDF characteristics.

REFERENCES

- [1] R. E. Dickinson, "Land surface processes and climate-surface albedos and energy balance," *Adv. Geophys.*, vol. 25, pp. 305–353, 1983.
- [2] A. Henderson-Sellers and M. F. Wilson, "Surface albedo data for climatic modeling," *Rev. Geophys.*, vol. 21, pp. 1743–1778, 1983.
- [3] D. Rechied, S. Hagemann, and D. Jacob, "Sensitivity of climate models to seasonal variability of snow-free land surface albedo," *Theor. Appl. Climatol.*, vol. 95, pp. 197–221, 2009.
- [4] D. Y. Hollinger *et al.*, "Albedo estimates for land surface models and support for a new paradigm based on foliage nitrogen concentration," *Glob. Change Biol.*, vol. 16, pp. 696–710, 2010.
- [5] V. Brovkin, L. Boysen, T. Raddatz, V. Gayler, A. Loew, and M. Claussen, "Evaluation of vegetation cover and land-surface albedo in MPI-ESM CMIP5 simulations," *J. Adv. Model. Earth Syst.*, vol. 5, pp. 48–57, 2013.
- [6] Y. Li, T. Wang, Z. Zeng, S. Peng, X. Lian, and S. Piao, "Evaluating biases in simulated land surface albedo from CMIP5 global climate models," *J. Geophys. Res., Atmos.*, vol. 121, pp. 6178–6190, 2016.
- [7] T. H. Tao, "Analysis of global land surface albedo climatology and spatial-temporal variation during 1981–2010 from multiple satellite products," *J. Geophys. Res., Atmos.*, vol. 119, pp. 10281–10298, 2014.
- [8] Y. Cao, S. Liang, T. He, and X. Chen, "Evaluation of four reanalysis surface albedo data sets in arctic using a satellite product," *IEEE Geosci. Remote Sens. Lett.*, vol. 13, no. 3, pp. 384–388, Mar. 2016.
- [9] C. B. Schaaf *et al.*, "First operational BRDF, albedo nadir reflectance products from MODIS," *Remote Sens. Environ.*, vol. 83, pp. 135–148, 2002.
- [10] F. Maignan, F. M. Bréon, and R. Lacaze, "Bidirectional reflectance of earth targets: Evaluation of analytical models using a large set of spaceborne measurements with emphasis on the hot spot," *Remote Sens. Environ.*, vol. 90, pp. 210–220, 2004.
- [11] M. Mira *et al.*, "The MODIS (collection V006) BRDF/albedo product MCD43D: Temporal course evaluated over agricultural landscape," *Remote Sens. Environ.*, vol. 170, pp. 216–228, 2015.
- [12] D. Rutan, F. Rose, M. Roman, N. Manalo-Smith, C. Schaaf, and T. Charlock, "Development and assessment of broadband surface albedo from clouds and the earth's radiant energy system clouds and radiation swath data product," *J. Geophys. Res., Atmos.*, vol. 114, Art. no. D08125, 2009.
- [13] D. Rutan, T. Charlock, F. Rose, S. Kato, S. Zentz, and L. Coleman, "Global surface albedo from CERES/TERRA surface and atmospheric radiation budget (SARB) data product," in *Proc. 12th Conf. Atmospheric Radiat.*, 2006, pp. 11–12.
- [14] J.-P. Muller, "Algorithm theoretical basis document ATBD, vol. 1: 4: BRDF/albedo retrieval," *MERIS AlbedoMaps*, vol. 1, pp. 1–19, 2006.
- [15] B. Geiger, L. Franchistéguy, D. Carrer, and J. L. Roujean, "Land surface analysis satellite application facility (LSA-SAF) product user manual (PUM) on albedo," Eumetsat, pp. 41, 2005.
- [16] W. J. D. V. Leeuwen and J. L. Roujean, "Land surface albedo from the synergistic use of polar (EPS) and geo-stationary (MSG) observing systems: An assessment of physical uncertainties," *Remote Sens. Environ.*, vol. 81, pp. 273–289, 2002.
- [17] Y. Govaerts and A. Lattanzio, "Retrieval error estimation of surface albedo derived from geostationary large band satellite observations: Application to meteosat-2 and meteosat-7 data," *J. Geophys. Res., Atmos.*, vol. 112, Art. no. D05102, 2007.
- [18] Y. Govaerts, A. Lattanzio, M. Taberner, and B. Pinty, "Generating global surface albedo products from multiple geostationary satellites," *Remote Sens. Environ.*, vol. 112, pp. 2804–2816, 2008.
- [19] D. Wang, S. Liang, T. He, and Y. Yu, "Direct estimation of land surface albedo from VIIRS data: Algorithm improvement and preliminary validation," *J. Geophys. Res., Atmos.*, vol. 118, pp. 12577–12586, 2013.
- [20] Y. Zhou, D. Wang, S. Liang, Y. Yu, and T. He, "Assessment of the Suomi NPP VIIRS land surface albedo data using station measurements and high-resolution albedo maps," *Remote Sens.*, vol. 8, 2016.
- [21] T. He, S. Liang, D. Wang, Q. Shi, and X. Tao, "Estimation of high-resolution land surface shortwave albedo from AVIRIS data," *IEEE J. Sel. Topics Appl. Earth Observ. Remote Sens.*, vol. 7, no. 12, pp. 4919–4928, Dec. 2014.
- [22] Y. Hu, G. Jia, C. Pohl, X. Zhang, and J. van Genderen, "Assessing surface albedo change and its induced radiation budget under rapid urbanization with landsat and GLASS data," *Theor. Appl. Climatol.*, vol. 123, pp. 711–722, 2016.
- [23] B. Pinty *et al.*, "Surface albedo retrieval from meteosat: 1 Theory," *J. Geophys. Res., Atmos.*, vol. 105, pp. 18099–18112, 2000.
- [24] Y. Shuai, J. G. Masek, F. Gao, and C. B. Schaaf, "An algorithm for the retrieval of 30-m snow-free albedo from landsat surface reflectance and MODIS BRDF," *Remote Sens. Environ.*, vol. 115, pp. 2204–2216, 2011.
- [25] B. Gao, L. Jia, and T. Wang, "Derivation of land surface albedo at high resolution by combining HJ-1A/B reflectance observations with MODIS BRDF products," *Remote Sens.*, vol. 6, pp. 8966–8985, 2014.
- [26] Z. Wang *et al.*, "Early spring post-fire snow albedo dynamics in high latitude boreal forests using landsat-8 OLI data," *Remote Sens. Environ.*, vol. 185, pp. 71–83, 2016.
- [27] Z. Wang *et al.*, "Monitoring land surface albedo and vegetation dynamics using high spatial and temporal resolution synthetic time series from Landsat and the MODIS BRDF/NBAR/albedo product," *Int. J. Appl. Earth Obs. Geoinformat.*, vol. 59, pp. 104–117, 2017.
- [28] Z. Jiao *et al.*, "The influence of spatial resolution on the angular variation patterns of optical reflectance as retrieved from MODIS and POLDER measurements," *Remote Sens. Environ.*, vol. 215, pp. 371–385, 2018.
- [29] T. He, S. Liang, D. Wang, X. Chen, D. X. Song, and B. Jiang, "Land surface albedo estimation from Chinese HJ satellite data based on the direct estimation approach," *Remote Sens.*, vol. 7, pp. 5495–5510, 2015.
- [30] R. Song, J. P. Muller, S. Kharbouche, F. Yin, and N. Gobron, "Validation of space-based albedo products from upscaled tower-based measurements over heterogeneous and homogeneous landscapes," *Remote Sens.*, vol. 12, 2020.
- [31] T. He *et al.*, "Evaluating land surface albedo estimation from landsat MSS, TM, ETM+, and OLI data based on the unified direct estimation approach," *Remote Sens. Environ.*, vol. 204, pp. 181–196, 2018.
- [32] X. Zhang *et al.*, "Development of the direct-estimation albedo algorithm for snow-free landsat TM albedo retrievals using field flux measurements," *IEEE Trans. Geosci. Remote Sens.*, vol. 58, no. 3, pp. 1550–1567, Oct. 2019.
- [33] Y. Guo, X. Wu, Y. Cheng, L. Wang, and T. Liu, "Maize recognition and accuracy evaluation based on high resolution remote sensing (GF-1) data," *Remote Sens. Inf.*, vol. 30, pp. 31–36, 2015.
- [34] Z. Li, "Application of GF-1 satellite in Land-use remote sensing monitoring," *Land Resour. Herald*, vol. 3, pp. 85–88, 2015.
- [35] H. Luo, F. Zi, L. Chen, W. Zhang, and S. Lu, "Application and prospect of GF-1 satellite in the field of land and resources," *Satell. Appl.*, vol. 03, pp. 41–43, 2015.
- [36] X. Li, *Spatial-Temporal Variability of Soil Moisture and Influencing Factors in Northwest Arid Area of China*. Beijing, China: Univ. Chinese Academy of Sciences, 2019.
- [37] X. Li *et al.*, "Watershed allied telemetry experimental research," *J. Geophys. Res., Atmos.*, vol. 114, 2009, Art. no. D22103.
- [38] C. B. Schaaf *et al.*, "First operational BRDF, albedo nadir reflectance products from MODIS," *Remote Sens. Environ.*, vol. 83, pp. 135–148, 2002.
- [39] E. Vermote, D. Tanre, J. Deuze, M. Herman, and J. Morcrette, "Second simulation of the satellite signal in the solar spectrum, 6S: An overview," *IEEE Trans. Geosci. Remote Sens.*, vol. 35, no. 3, pp. 675–686, May 1997.
- [40] A. Chen, L. Bian, and Y. Liu, "Deriving albedo over cloudy areas with composite inversion," in *Proc. SPIE, Geoinformatics*, Nanjing, China, 2007, Art. no. 65337.
- [41] W. Lucht, C. B. Schaaf, and A. H. Strahler, "An algorithm for the retrieval of albedo from space using semiempirical BRDF models," *IEEE Trans. Geosci. Remote Sens.*, vol. 38, no. 2, pp. 977–998, Mar. 2000.

- [42] S. Liang, "A direct algorithm for estimating land surface broadband albedos from MODIS imagery," *IEEE Trans. Geosci. Remote Sens.*, vol. 41, no. 1, pp. 136–145, Jan. 2003.
- [43] S. Liang, "Narrowband to broadband conversions of land surface albedo I: Algorithms," *Remote Sens. Environ.*, vol. 76, pp. 213–238, 2001.
- [44] S. Liang, X. Li, and J. Wang, *Quantitative Remote Sensing: Concept and Algorithm*. Beijing, China: Science Press, 2013.
- [45] A. Cescatti *et al.*, "Intercomparison of MODIS albedo retrievals and in situ measurements across the global FLUXNET network," *Remote Sens. Environ.*, vol. 121, pp. 323–334, 2012.
- [46] A. E. Tekeli, A. Şensoy, A. Şorman, Z. Akyürek, and Ü Şorman, "Accuracy assessment of MODIS daily snow albedo retrievals with in situ measurements in Karasu Basin, Turkey," *Hydrological Processes*, vol. 20, pp. 705–721, 2006.
- [47] S. Liang, J. S. And, and J. E. Box, "Mapping daily snow/ice shortwave broadband albedo from moderate resolution imaging spectroradiometer (MODIS): The improved direct retrieval algorithm and validation with Greenland in situ measurement," *J. Geophys. Res., Atmos.*, vol. 110, no. D10, May 2005, Art. no. D10109.
- [48] L. Feng, J. Li, W. Gong, X. Zhao, X. Chen, and X. Pang, "Radiometric cross-calibration of Gaofen-1 WFV cameras using landsat-8 OLI images: A solution for large view angle associated problems," *Remote Sens. Environ.*, vol. 174, pp. 56–68, 2016.



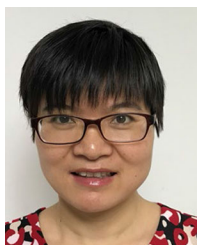
Tao He (Member, IEEE) received the B.E. degree in photogrammetry and remote sensing from Wuhan University, Wuhan, China, in 2006, and the Ph.D. degree in geography from the University of Maryland, College Park, MD, USA, in 2012.

He is a Professor with the School of Remote Sensing and Information Engineering, Wuhan University and also with the Department of Geographical Sciences, University of Maryland. His research interests include surface anisotropy and albedo modeling, data fusion of satellite products, and long-term regional and global surface radiation budget analysis.



Huawei Wan received the Ph.D. degree from Beijing Normal University, Beijing, China.

She is currently a Research Scientist with the Center for Satellite Application on Ecology and Environment, Ministry of Ecology and Environment, Beijing, China. Her research interests include quantitative parameters reversion and ecosystem and biodiversity assessment based on remote sensing.



Hongmin Zhou (Member, IEEE) received the Ph.D. degree from Beijing Normal University, Beijing, China, in 2018.

She is currently a Senior Engineer with the State Key Laboratory of Remote Sensing Science, Faculty of Geographical Sciences, Beijing Normal University/Chinese Academy of Sciences. Her research interests include land surface radiation budget, land surface parameters retrieval from various remotely sensed data, and land surface products validation.



Zhe Wang received the B.S. degree from the Suzhou University of Science and Technology, Jiangsu, China, in 2019. She is currently working toward the M.S. degree with Henan Polytechnic University, Jiaozuo, China.

Her research interests include land surface parameters retrieval and land surface products validation.



Wu Ma received the B.S. degree from the Nanjing University of Information Science and Technology, Nanjing, China, in 2018. She is currently working toward the master's degree with Beijing Normal University, Beijing, China.

Her research interests include the scale effect and scale conversion of BRDF model parameters.

Jindi Wang received the B.S. degree from the Beijing University of Posts and Telecommunications, Beijing, China, in 1982.

She is currently a Professor with the State Key Laboratory of Remote Sensing Science, Research Center for Remote Sensing and Geographic Information Systems, Beijing Normal University, Beijing, China. Her primary research interests focus on land surface bidirectional reflectance distribution function modeling, land surface parameter retrieval, and typical land surface objects' spectrum library building and its application.



Shunlin Liang (Fellow, IEEE) received the Ph.D. degree from Boston University, Boston, MA, USA.

He is a Professor with the Department of Geographical Sciences, University of Maryland, College Park, MD, USA. He has authored or coauthored more than 390 SCI indexed peer-reviewed journal articles, 42 book chapters, and nine special issues on different journals. He authored/edited seven books and four of which were translated in Chinese, such as *Quantitative Remote Sensing of Land Surfaces* (Wiley, 2004), *Advances in Land Remote Sensing: System, Modeling, Inversion and Application* (Springer, 2008), *Advanced Remote Sensing: Terrestrial Information Extraction and Applications* (Academic Press, 2012, 2019), *Global Land Surface Satellite (GLASS) Products: Algorithms, Validation and Analysis* (Springer, 2013), *Land Surface Observation, Modeling and Data Assimilation* (World Scientific, 2013), and *Earth's Energy Budget* (Elsevier, 2017). He has led a team to develop the GLASS products that are publicly available at www.glass.umd.edu and widely used. He was the Editor-in-Chief for the nine-volume books titled *Comprehensive Remote Sensing* (Elsevier, 2017). His main research interests focus on estimating land surface variables from satellite data, global satellite product generation, Earth's energy balance, and environmental changes.

Dr. Liang was an Associate Editor for IEEE TRANSACTIONS ON GEOSCIENCE AND REMOTE SENSING and is currently the Editor-in-Chief for *Science of Remote Sensing*.